ACS APPLIED MATERIALS & INTERFACES

www.acsami.org

Research Article

Unveiling Nanoscale Ordering in Amorphous Semiconducting Polymers Using Four-Dimensional Scanning Transmission Electron Microscopy

Gabriel A. Calderón Ortiz, Menglin Zhu, Andrew Wadsworth, Letian Dou, Iain McCulloch, and Jinwoo Hwang*

Cite This: *ACS Appl. Mater. Interfaces* 2024, 16, 55852−55863

Read Online

ACCESS | Metrics & More | Article Recommendations

ABSTRACT: We present four-dimensional (4D) scanning transmission electron microscopy (STEM) analysis to obtain a high level of detail regarding the nanoscale ordering within largely disordered organic semiconducting polymers. Understanding nanoscale molecular ordering in semiconducting polymers is crucial due to its connection to the materials' important properties. However, acquiring such information in a spatially localized manner has been limited by the lack of a nanoscale experimental probe, weak signal from ordering, and radiation damage to the sample. By collecting nanodiffraction patterns with a high dynamic range pixelated detector, we acquired statistically robust, high signal-to-noise ratio diffraction patterns from semiconducting organic materials, including poly(3-hexylthiophene-2,5-diyl) (P3HT), P3HT/[6,6]-phenyl C61 butyric acid methyl ester, and indacenodithiophene-*co*-benzothiadiazole (IDTBT), which largely have disordered structures. Real-space images of the ordered domains were reconstructed from the 4D-STEM data set for a variety of scattering vectors and in-plane angles to capture the different molecular stacking distances and their in-plane orientation. These were then analyzed to obtain the average size of the ordered domains within the sample. Such measurements were arranged in a two-dimensional (2D) histogram, which showed a direct relationship between the type and size of molecular ordering. Complementary analyses, such as intensity variance and angular correlation, were applied to obtain ordering and symmetry information. These analyses enabled us to directly characterize the alkyl and $\pi-\pi$ stacking of P3HT, as well as the fullerene domains caused by donor segregation in the P3HT sample. Furthermore, the analysis also captured changes in the P3HT domains when the fullerenes are incorporated. Lastly, IDTBT showed a much lesser degree of ordering without much disinclination between the domains within the 2D histogram. The 4D-STEM analysis that we report here unveils new details of molecular ordering that can be used to optimize the properties of this important class of materials.

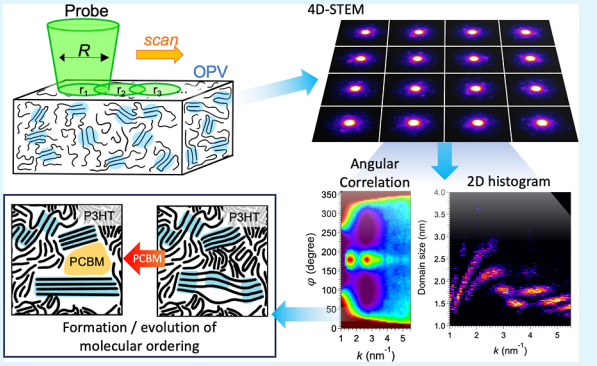

KEYWORDS: *4D-STEM, molecular ordering, organic photovoltaics, P3HT, IDTBT*

1. INTRODUCTION

The properties of organic semiconductors can be significantly influenced by the alignment of molecules within the material. More specifically, the details of the ordering between polymer molecules—such as the type, orientation, size, and volume fraction of the ordered domains—are crucial parameters to determine in order to understand the exact structure−property relationships at the nanometer scale in these systems.[1] This is especially important for systems that are neither completely amorphous nor crystalline, for example, poly(3-hexylthiophene-2,5-diyl) (P3HT) and indacenodithiophene-*co*-benzothiadiazole (IDTBT) copolymer, which have been known for their high performance. Their important properties, such as carrier mobility, are highly dependent on the subtle ordering of molecules at the nanometer scale.[2,3] Previous theoretical and experimental studies have highlighted the importance of characterizing nanometer-scale molecular ordering and the significant role it plays in bulk heterojunctions,[4−6] which greatly affects targeted properties such as solar cell efficiency that has been gradually improving but still remains less than ∼20%.[7]

Previous characterization of molecular ordering has been mainly performed with grazing incidence wide-angle X-ray

Received: July 6, 2024
Revised: September 16, 2024
Accepted: September 20, 2024
Published: October 4, 2024

scattering (GIWAXS).[1,8] Studies have been conducted with varying parameters such as molecular weight, deposition methods,[9] different polymer designs,[10] and physically induced ordering, such as by rolling the polymer film[11] or depositing the film on polymer substrates with a crystallographic orientation.[12] With the high coherence of X-ray illumination, GIWAXS can show the overall degree of molecular ordering, and the results have been compared to important properties such as absorption characteristics,[12,13] crystallization behavior,[14] charge mobility,[15] and device performance.[16] However, GIWAXS uses a large beam size, typically about a few hundred microns or larger.[17] This means that the information is averaged over the entire illuminated area, making it difficult to acquire spatially resolved information about nanoscale morphology or molecular ordering within the bulk heterojunction. This limitation has made it difficult to study the spatial distribution of different types of molecular ordering, the blending between the donor and acceptor molecules, and the size and volume fractions of the ordered domains.

Transmission electron microscopy (TEM), on the other hand, uses much smaller probes and therefore provides a high site specificity that larger area diffraction methods cannot offer. High-resolution TEM (HRTEM) imaging can, in some cases, reveal the details of molecular ordering, such as their stacking type, especially in the case of small molecule systems where the molecules are highly crystallized.[18] However, the HRTEM method is difficult to use for polymer systems, where the degree of molecular ordering is substantially low. Selected area electron diffraction has also been used for crystallized polymers to get the crystallographic information as well as their behavior.[19] Meanwhile, dark-field imaging that utilizes the diffracted beam intensity either in TEM[10] or scanning TEM (STEM)[20] mode has shown to be effective in visualizing the ordered domains in some selected polymers without causing radiation damage,[21] but it is still difficult to determine the quantitative information about the ordering, such as their sizes and volume fraction in general. Recently, scanning nanobeam diffraction in STEM (also known as four-dimensional STEM, or 4D-STEM) utilizing the fast pixelated STEM detector has shown some quantitative information, such as the orientation[22,23] in highly crystallized systems[24,25] and even semicrystalline polymers[26] and a molecular glass system.[27] However, the 4D-STEM method shares similar issues as in dark-field TEM imaging, and therefore, advancing it to more disordered systems, such as polymer blends in bulk heterojunctions, has remained challenging. In addition, all TEM-based methods share a common challenge of controlling electron radiation damage to the sample, which requires optimizing the dose and electron acceleration voltage for the particular system and sample under investigation.

As mentioned above, while both X-ray and TEM-based methods provide valuable information about the ordering in organic semiconductors, they show limitations in determining important quantitative details such as the size, distribution, and volume fraction of subtle molecular ordering at the nanoscale that correlate directly to the charge transport and solar cell efficiency of these systems. This is especially true in polymer systems, where the degree of ordering is relatively low and therefore difficult to detect. These limitations have created a knowledge gap in the structure−property relationships in these systems that should be filled in order to achieve further breakthroughs in these novel classes of materials.

In this article, we present a new method for identifying and quantifying molecular ordered domains at the nanoscale in organic semiconducting polymers using quantitative analysis of nanodiffraction patterns from 4D-STEM. Our 4D-STEM uses electron beams that probe individual nanoscale areas of the sample over a large sample area, providing both nanoscale site specificity and spatial sampling rates sufficiently high to deliver statistically reliable information on the details of the structure of molecular ordering in polymer systems. A large number of diffraction patterns from nanoscale ordering are recorded using a high dynamic range fast STEM detector[28] that is capable of 32 bit depth and therefore achieves a high signal-to-noise ratio, which is crucial for the analysis of subtle diffraction signals. Three different analysis methods are applied to the 4D-STEM data: intensity variance, angular correlation, and two-dimensional (2D) histogram analysis, to extract quantitative information about the nanoscale ordering, including their types and size distribution. P3HT and P3HT/[6,6]-phenyl C61 butyric acid methyl ester (P3HT/PCBM) are well-suited for the study of molecular ordering as a model system due to their high performance, which is directly related to their nanoscale morphology. We also studied IDTBT, which lacks ordering yet produces higher carrier mobility.[29,30] In situ annealing in STEM was performed to remove residual solvents that were used for the deposition of the thin films, which helps minimize unwanted effects such as carbon contamination and radiation damage upon illumination of the sample. 4D-STEM results show that the molecular ordering has different types at the nanometer scale in P3HT, each forming with distinctive intermolecular distances and domain sizes, which change upon mixing with acceptor molecules such as PCBM. On the other hand, in the case of IDTBT, results indicate no presence of distinctive molecular domains at the nanoscale, as opposed to P3HT. The new data we report here provide detailed information about the structural parameters in polymer-based organic semiconductor systems, which can help establish new structure−property relationships and lead to further breakthroughs in their performance.

2. EXPERIMENTAL DETAILS

2.1. TEM Sample Preparation. P3HT and IDTBT were synthesized using the methods reported previously.[31,32] Polymer films were deposited by using spin coating. P3HT (20 mg/mL), P3HT/PCBM (20 mg/20 mg/mL), and IDTBT (10 mg/mL) were dissolved in dichlorobenzene and spin-coated on a glass slide for P3HT and P3HT/PCBM, while IDTBT was spin-coated at 1000 rpm for 1 min using a Laurell WS-400B-6NPP-Lite Spinner. A gold cap was deposited over every thin film sample by using a Pelco model 3 sputter coater 91,000 to serve as a protective layer during the TEM sample preparation. Cross-sectional TEM samples were prepared for all three systems using a focused ion beam (FIB) Helios NanoLab 600 DualBeam. FIB milling was done in two different voltages in sequence, 30 and 5 keV, and the milling angles were optimized to ensure minimized damage to the polymer film. This method has been previously used for organic films and showed that the molecular ordering can remain intact after milling without any significant amorphization.[18] Cross-section FIB samples were deliberately made to have an approximate thickness of about 100 nm, which was measured using electron transmittance of the sample,[33] to ensure there is enough diffraction signal generated from the film. FIB milling can affect the surface structure, and it is widely known that surface damage can be around a few nanometers in thickness. Such potential surface damage, however, would have a minor influence on the structure we measure from the "bulk" of the TEM foil. Plasma cleaning of the TEM samples is not suitable for our OPV samples

https://doi.org/10.1021/acsami.4c11198
ACS Appl. Mater. Interfaces 2024, 16, 55852−55863

since it may destroy the molecular structure. Instead, we annealed the TEM samples in situ to remove hydrocarbons from the surface of the sample. In situ annealing was performed with a Gatan heating TEM holder at 130 °C for 1 h for P3HT-based systems and 100 °C for 1 h for IDTBT. The annealing temperature is similar to that commonly used for film degassing and reducing recombination in device fabrication.[16,34] In our case, in addition to producing a sample with conditions closer to actual devices, the annealing also helps remove any solvent molecules and hydrocarbons trapped within the foil, which, according to our observation, tend to exacerbate carbon contamination and radiation damage upon illumination with the electron beam. As we will show in the results section, the removal of hydrocarbons from the surface greatly helped reduce both the carbon contamination and radiation damage of the samples.

2.2. TEM Experiment. *2.2.1. Suppressing Radiation Damage.* In addition to the in situ annealing to remove residual solvents (explained above), the acceleration voltage, beam current, beam size, and degree of overlap between the probed areas were collectively adjusted to reduce potential radiation damage to the sample. Previous TEM works on OPVs have shown that, despite the possibility of both knock-on and ionization-type damages under electron illumination,[35] proper optimization of beam dose as well as acceleration voltages has shown to be effective in preventing radiation damages. To minimize radiation damage in this work, each of the parameters that may contribute to the damage, namely, the acceleration voltage, beam dose, and probe grid positions, was carefully examined one by one.

2.2.1.1. Acceleration Voltage. In general, higher acceleration voltages create more knock-on damage, while lower acceleration voltages contribute more to ionization damage (especially in organic materials).[36] However, it has not been clear which damage mechanism is more dominant in OPVs. For example, some of the previous works have used lower voltage (80 keV),[37] while others used voltages as high as 300 keV.[37,38] For the polymer systems that we studied, we found that both low and high voltages can be used without any significant radiation damage or carbon contamination, as long as the in situ annealing is done (explained in Section 2.2), and the beam dose is optimized (an example of the damage test will be shown and explained below), although the results vary slightly depending on the materials that we studied. The optimized voltages that led to the minimized beam-induced carbon contamination were 80 keV for P3HT-based systems and 200 keV for IDTBT, so the resulting data sets were subsequently used for the analysis.

2.2.1.2. Beam Dose. The analysis that we performed, including intensity variance analysis and the calculation of ordering size distribution, requires a high signal-to-noise ratio,[39] and therefore we ensured the average counts in the first ring area in the diffraction pattern (k = 2.7 nm^{-1}) recorded on the pixelated detector to be about 2,800 counts (Figure 1a), which is above the minimum counts required for variance calculation,[40] by optimizing the beam current, even at higher voltages where there is less scattering due to the decreased cross section. Scattering cross section also changes depending on the materials; therefore, the optimization led to the use of the beam current of 0.1 nA for P3HT (at 80 keV) and 0.08 nA for IDTBT (at 200 keV).

2.2.1.3. Probe Grid Positions. Since our purpose was to measure diffraction patterns continuously across the sample area, the probe positions needed to have some degree of overlapping to ensure that no area is missed. However, overlapping of the probe position more than needed would result in overexposure of one area to the beam and that would in turn effectively increase the dose. Therefore, we optimized the probe positions to have 50% overlap in terms of the diameter of the circular area (which is the 2 nm probe size used), as shown in Figure 1b. In addition, all areas were scanned only once to ensure no effect from radiation damage.

By simultaneously optimizing all three parameters mentioned above, we have tested the degree of radiation damage as well as carbon contamination before and after data acquisition at different voltages. The result from 300 keV is shown in Figure 1c as an example. No significant beam damage was visible after data acquisition, but a small degree of contamination was observed.

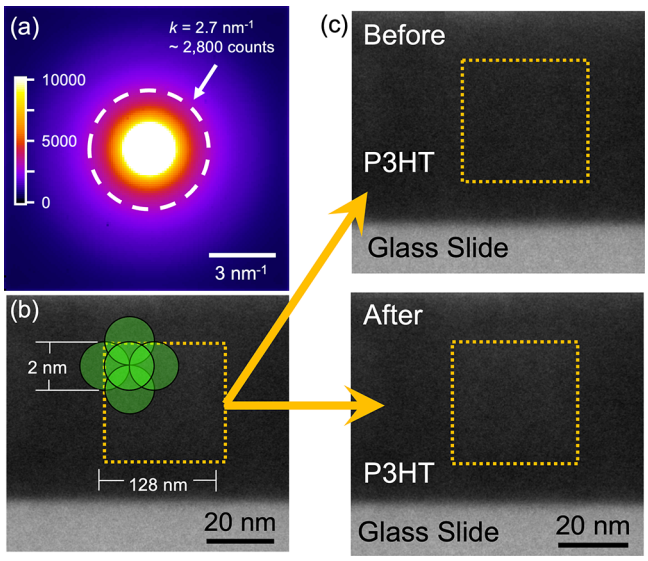

Figure 1. (a) Averaged nanodiffraction over a sample area showing the intensity at the first peak area (k = 2.7 nm^{-1}) being ~2,800 counts. (b) Cross-section HAADF image of P3HT. The dashed square is the area where the probes were scanned over for 4D-STEM measurement. The green circles (not to scale) schematically depict the probe positions to show the scheme of the overlapping of their positions during the scan. (c) HAADF images showing scanned areas of P3HT before (top) and after (bottom) the data acquisition at 300 keV. There is about a 7% increase in the average intensity within the yellow dotted box, between the before and after 4D-STEM scans.

However, since each area was scanned only once, we safely assumed that the degree of contamination does not affect the quality of our data significantly.

2.2.2. 4D-STEM Acquisition of Nanodiffraction. An Electron Microscopy Pixel Array Detector with 128 by 128 pixels and a 32 bit dynamic range[28] was used to collect the 4D-STEM data. To maximize the signals from the local ordering, it has been shown previously that the probe size needs to be comparable to the size of the ordering, and when it is, the intensity variance (explained below) can be maximized.[40] Based on this theorem, we determined the probe size by performing a series of nanodiffraction acquisitions with varying probe sizes from 1 to 5 nm, which revealed that a 2 nm probe size is the most adequate for the measurement. The 2 nm probe size also provides a good balance between the real-space and reciprocal-space resolution. In contrast, a 1 nm probe size would increase real-space resolution, but due to the increased convergence angle, the reciprocal-space resolution would decrease, leading to smaller distinctions in the peak positions in the resulting angular correlation and ordering maps. The beam current was set to be ~0.1 nA with a probe dwell time of 1 ms, which provided enough signal for the analysis (shown in Figure 1a). The probe was scanned over the sample area from the cross-section view of the sample with 256 × 256 grid positions (Figure 2a). With the 50% overlapping of the probe positions that we explained above, this typically corresponds to about 128 nm × 128 nm in the area (yellow box in Figure 1b). As a result, one scan should generate 256 × 256 = 65,536 patterns, but we remove the patterns at the top and bottom edges of the scanned area to ensure no signal from the nearby area is captured, either from the substrate at the bottom or the gold layer that we deposited at the top of the OPV film. This typically leaves about 49,000 nanodiffraction patterns per area. The nanodiffraction patterns were analyzed using three different analysis methods: intensity variance analysis, angular correlation analysis, and 2D histogram of ordering size distribution, which we explain in detail below.

2.2.3. Intensity Variance Analysis. Intensity variance analysis calculates the normalized variance of the diffracted intensity as a function of scattering angle as well as probe size.[41−43] More generally

https://doi.org/10.1021/acsami.4c11198
ACS Appl. Mater. Interfaces 2024, 16, 55852−55863

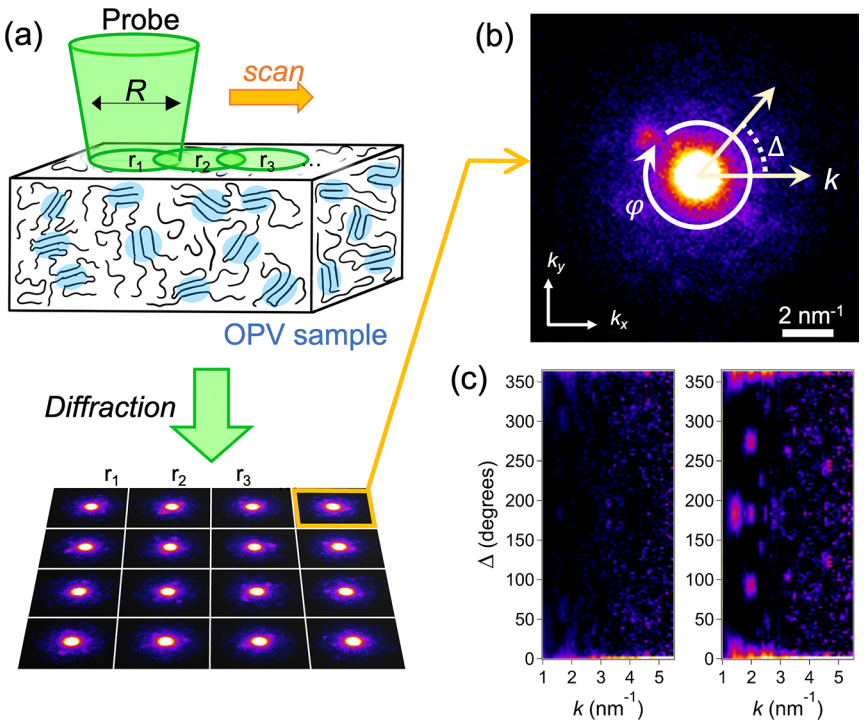

Figure 2. (a) Schematic of 4D-STEM in this work. The electron probe generates one nanodiffraction pattern per probe position (**r**) and scans over the sample typically with 256 by 256 grid positions, generating ~65,000 patterns per scanned area. (b) Example nanodiffraction pattern with notations used for the intensity variance (eq 1) and angular correlation (eq 2) analyses. (c) Example angular correlation functions calculated from two different nanodiffraction patterns. The one on the right shows much clearer rotational symmetry, indicating a high degree of molecular ordering in that area. The one on the left, on the other hand, does not show any clear symmetry.

known as fluctuation microscopy,[44,45] this method yields intensity variance (V) as a measure of structural fluctuation at the length scale of the probe size (R) in disordered materials. V is calculated from each of the ~49,000 nanodiffraction patterns that we collected from one sample as explained in the previous section. Typically, each 2D pattern is annular-averaged (over the φ angle shown in Figure 2b) to make it intensity (I) vs scattering vector magnitude (k). Then V is calculated using eq 1

$$V(k, R) = \frac{\langle I^2(k, R, \mathbf{r})\rangle_{\mathbf{r}}}{\langle I(k, R, \mathbf{r})\rangle_{\mathbf{r}}^2} - 1 \quad (1)$$

where $< >_{\mathbf{r}}$ indicates the averaging over the probe position ($\mathbf{r}$) and R is the probe size (R = 2 nm with 2.6 mrad convergence angle at 80 keV). Qualitatively, high V means that there is high structural fluctuation at the length scale of R, which indicates high structural heterogeneity due to the presence of local ordering that diffracts to that certain k value. Just as in any diffraction measurement, k is related to the inverse of the "interplanar spacing" between the ordering, and therefore, it relates to the internal structure (or type) of the ordering. Since the diffraction is expected to be generated by the molecular ordering in OPVs, our general expectation is that the k value should be the inverse of the interplanar distance (d) between the molecules ($k = 1/d$). The d value changes as the type of the molecular ordering (stacking) changes,[46] and therefore, k is an important parameter to differentiate the types of the local ordering as we will explain in more detail later.

2.2.4. Angular Correlation Analysis. Angular correlation, C, calculates the autocorrelation between the diffraction intensities as a function of the annular angle (Δ) in each nanodiffraction pattern at one k

$$C_k(\Delta) = \frac{\langle I_k(\varphi) I_k(\varphi + \Delta)\rangle_\varphi - \langle I_k(\varphi)\rangle_\varphi^2}{\langle I_k(\varphi)\rangle_\varphi^2} \quad (2)$$

where $< >_\varphi$ indicates the averaging over all φs (see Figure 2b). We calculate $C_k(\Delta)$ for all ks to get $C(\Delta)$, and averaging $C(\Delta)$ over the entire stacks of diffraction patterns from the area will provide statistically significant information about what types of structural (rotational) symmetry are dominant within that area of the disordered sample.[47−50] Typically, 2-fold symmetry is dominant in $C(\Delta)$ since one diffracted beam always has its conjugate (known as Friedel symmetry). In addition, any crystals, including organic crystals, can show higher-order symmetries. For example, higher-order symmetries, such as 4-, 5-, and 6-fold symmetries, have been measured in amorphous metals where atoms tend to be more close-packed.[42] However, due to the large molecule size and structural disorder (e.g., bending and distortion of the molecules), we expect that the higher-order symmetry will be low in $C(\Delta)$ from OPVs. Instead, it is likely that $C(\Delta)$ will mostly have dominant 2-fold symmetry, and the 2-fold signal will be used as an important parameter representing the degree of ordering within the material, complementing the information from V that we explained above.

2.2.5. 2D Histogram of Ordering Size Distribution. The average size of the local ordering was analyzed for different k values (i.e., ordering types), and the result was plotted in the form of a 2D histogram using the method reported in Im et al.[48] Since 4D-STEM generates the 2D nanodiffraction patterns from the entire 2D real-space area scanned with the probe, we can reconstruct the real-space image of the area using any pixel or any subarea of the reciprocal space.[42] If we use the reciprocal space pixel (or area) near the k value that has a diffraction peak generated from a certain ordering type, the resulting reconstructed image will show the areas where that ordering is present.[48] This is fundamentally similar to TEM dark-field imaging of different grains in polycrystalline materials but with two major differences. One is that the signals from molecular ordering are much weaker than what you would expect from a crystalline grain because the degree of local ordering is very small and still contains substantial disorder. The other is a technical difference: the use of the virtual aperture (meaning the pixel chosen in the reciprocal space) in our

https://doi.org/10.1021/acsami.4c11198
ACS Appl. Mater. Interfaces 2024, 16, 55852−55863

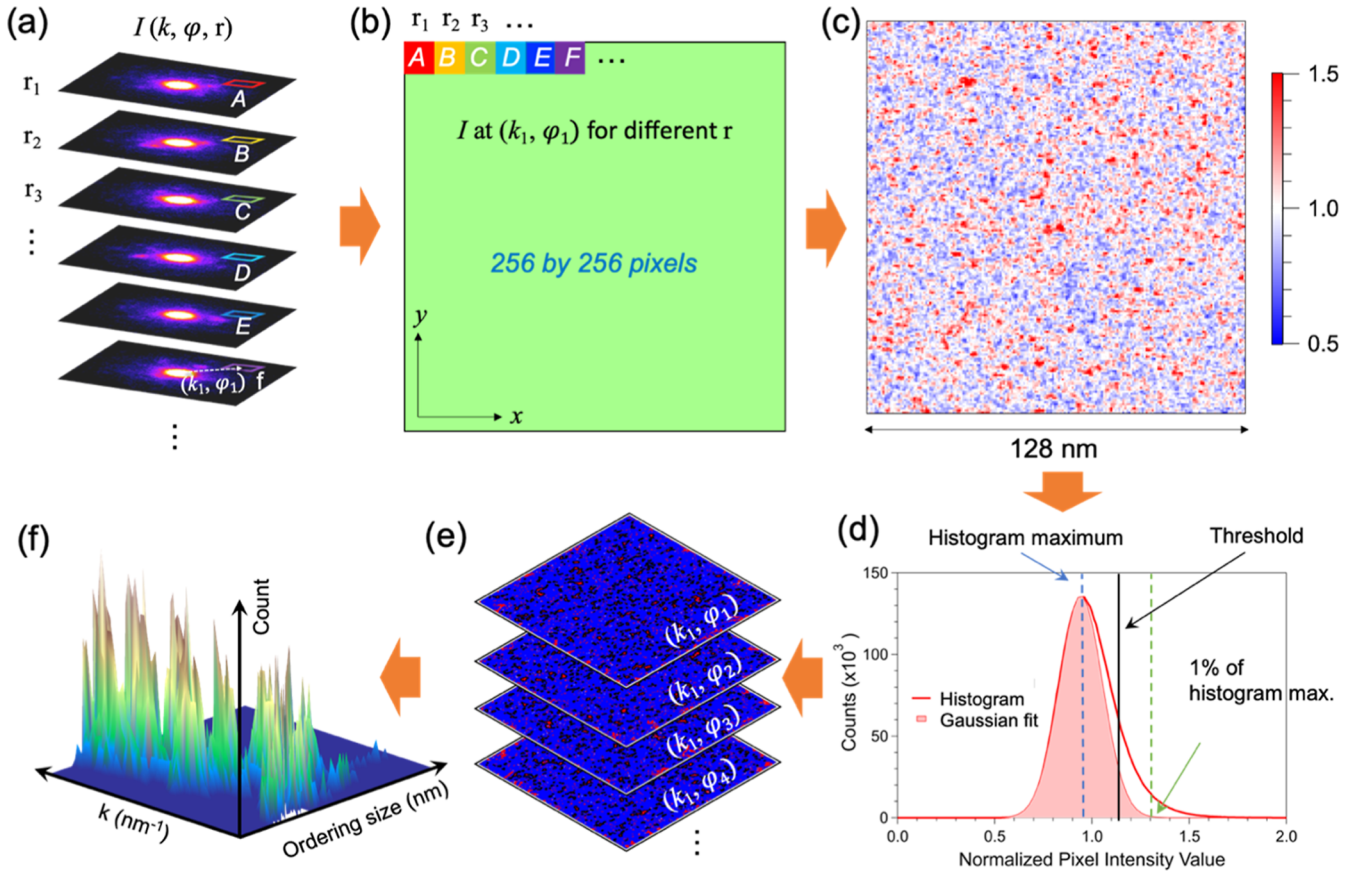

Figure 3. Process of ordering size determination. (a) Series of nanodiffraction patterns, $I(k, \varphi)$, acquired at different probe positions, r. (b) For a particular (k_1, φ_1), the intensities of the corresponding pixels (A, B, C,...) are reconstructed into the same grid position as the probe position. (c) Example of a reconstructed image showing high intensity areas (shown in red) representing the diffracting ordered domains. (d) Intensity histogram from all images (with φ_1–φ_{126}) with the same k and Gaussian fitting to determine the threshold value. (e) Stacks of images with the threshold mask applied for all φs. (f) 2D histogram of the number (count) of the ordered domains for their size and k.

4D-STEM method enables sampling of all possible in-plane angles per each k value, which is practically very challenging in dark-field TEM.[51]

The general procedure to make 2D histograms is shown in Figure 3. First, from the diffraction patterns (I) acquired from different probe positions ($\mathbf{r}$), which is $I(k, \varphi, \mathbf{r})$ shown in Figure 3a, we reconstruct the 2D map of I using the grid positions of $\mathbf{r}$ that we used in the experiment for a certain k and φ (Figure 3b). An example of this reconstructed image is shown in Figure 3c. To remove any unwanted effects from the small variation of TEM foil thickness between the areas, each of these reconstructed images was normalized by the average intensities of all pixels in that image. The reconstructed images typically contain small pixel-to-pixel noise that is irrelevant to the measurement of local ordering size, so we applied a Gaussian convolution (with a 3 × 3 Gaussian kernel) to denoise the data.[52] As shown in Figure 3c, the small local regions with high intensity correspond to the area where the diffraction intensity is high, and therefore, those regions (domains) correspond to the area where local ordering is present, with their types represented by the k value of the reconstructed image. For each k value, we construct the intensity histogram utilizing all reconstructed images along φ, shown in Figure 3d. The histogram typically has a longer tail to the high intensity side (right side), which indicates that the higher intensities are generated by diffraction from local regions. To quantify the average size of the local ordered domains from those images, we first fit a Gaussian function to the left side of the histogram[48] and applied an intensity threshold mask, with the threshold value determined at the middle point between the intensities (x axis) at the Gaussian maximum and the 1% of the Gaussian maximum. The threshold masking is applied to every image with different φs along the annular direction (Figure 3e) with the same scattering vector. Since the images are pixelated, we typically get a total of 126 φ values per k. Then, the process is repeated for all ks. The result is then summarized in a 2D histogram that shows the number (count) of the ordered domains by their size (diameter, with the assumption that the domains are roughly spherical in their shape) as well as their k (Figure 3f).

3. RESULTS AND DISCUSSION

3.1. Types and Size of Molecular Ordering in P3HT and P3HT/PCBM.

3.1.1. Poly(3-hexylthiophene-2,5-diyl). Figure 4a,b shows the 2D histograms of the size (diameter) of the ordered regions measured using the method described in Section 2.2.5, for different k values. They show the number of ordered regions (the color scale count) that have a certain domain size (left y axis) for a particular k value (x axis), which is the inverse of the intermolecular spacing within the ordered domain that is at Bragg condition. The 2D histogram for P3HT in Figure 4a shows the "hotspots" (*i.e.*, the local spots that have a high color scale count) at certain k values (indicated as B–I), which indicates that there are distinct types of molecular ordering, and those ordered domains are at (or near) Bragg conditions and therefore diffract more strongly than the amorphous matrix. Each hotspot spans over a certain range of k, which indicates that the intermolecular stacking within each ordered region is not completely uniform, potentially due to the bending or distortion of the molecules, which is likely to happen because of the relatively flexible nature of these molecules. Each type of ordering also has a

https://doi.org/10.1021/acsami.4c11198
ACS Appl. Mater. Interfaces 2024, 16, 55852–55863

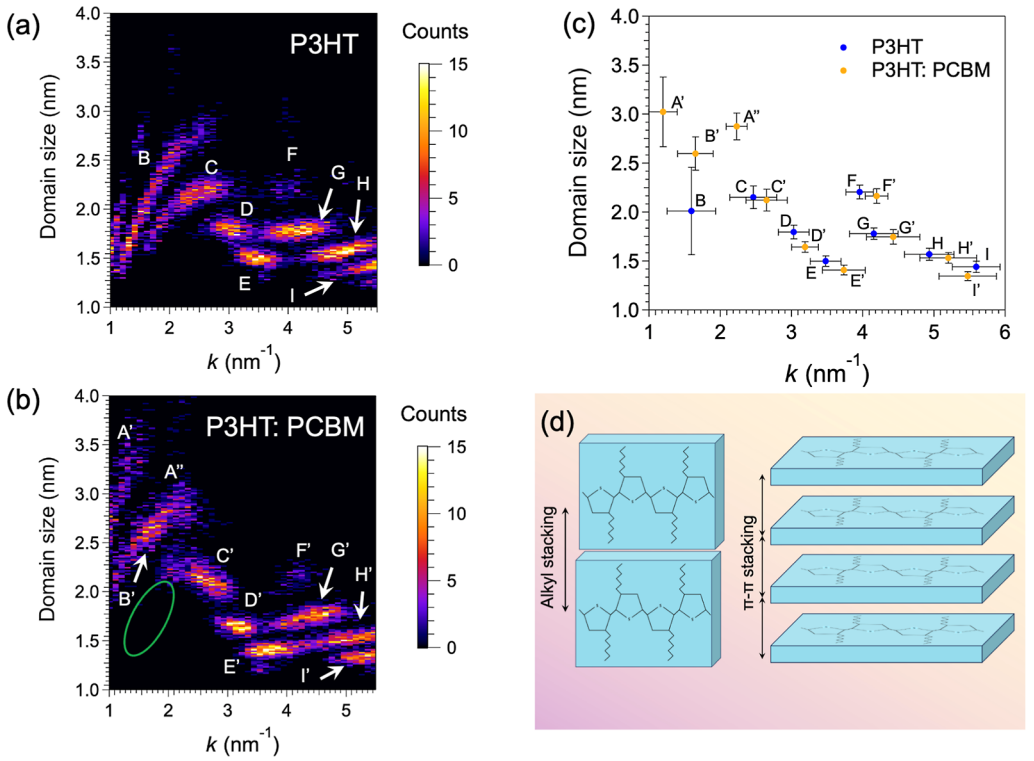

Figure 4. 2D histogram of domain size (diameter) for (a) P3HT and (b) P3HT/PCBM as a function of k. (c) Domain size vs k from both P3HT and P3HT/PCBM determined from (a) and (b). (d) Schematic of alkyl and $\pi-\pi$ stacking shown using P3HT polymer chains.

certain size range, which means that the region that has a particular stacking of molecules tends to show certain sizes in the projected dark-field image. The 2D size histogram from 4D-STEM shown in Figure 4a therefore provides important new information about the molecular ordering: (i) it resolves the types of nanoscale ordering which potentially indicate the different stacking types of the molecules, and (ii) an ordered region with specific molecular stacking types has a characteristic size when it is spatially oriented to the Bragg condition. These are the types of information that are not captured in GIWAXS which inherently averages the signals over the large probed volume.

The next question is then what exact molecular stacking types give rise to the k peak positions of the hotspots shown in Figure 4a. By comparison of their k positions to the known ordering types, the types of some of the hotspots can be identified. First, the hotspot C in Figure 4a that centers at $k \sim 2.5$ nm^{-1} can be correlated to the well-known $\pi-\pi$ stacking of P3HT (Figure 4d), which has the peak position at $k \sim 2.6$ nm^{-1} as found from GIWAXS.[16] The average size of the ordered domains (that are aligned to the Bragg condition) of $\pi-\pi$ stacking is 2.2 ± 0.3 nm. Second, the long line that spans over the k range of ~1 to 2.2 nm^{-1} (indicated as B in Figure 4a) can be identified as the alkyl stacking of P3HT molecules (Figure 4d). Unlike the GIWAXS data that showed two distinct peaks at $k \sim 1.2$ and 1.9 nm^{-1} for alkyl stacking,[16] the fact that the alkyl hotspot is extended over the k range of ~1 to 2.2 nm^{-1} in Figure 4a suggests that alkyl stacking in our film has a range of stacking distances, and their sizes (which has the range of ~1.5 to 2.7 nm) vary depending on the stacking distance. The wide range in the alkyl stacking distance can be explained by the effect of side chains on the ordering. Unlike the $\pi-\pi$ stacking, alkyl stacking in P3HT can be significantly affected by the way the side chains of different molecules interact with each other. For example, if the side chains are either compressed or interdigitated along the direction of alkyl stacking, then the alkyl stacking distance between the backbone of the polymer chains will be smaller, leading to the higher-bound k values (up to ~2.7 nm^{-1}) for the hotspot B. On the other hand, if the side chains are not interdigitated or compressed, then the distance between the chains along the alkyl stacking will be larger, leading to the lower-bound k values (~1.5 nm^{-1}). A similar argument can be used to explain the extension of the $\pi-\pi$ hotspot C that is extended to the lower k (and smaller size).

The hotspots D–H, on the other hand, do not have any corresponding peaks in typical diffraction data generated by GIWAXS. The spots D–I show their k values of ~3 to 6 nm^{-1}, which corresponds to very short real-space distances of ~2 to 3 Å. In addition (as we will explain in detail in Section 3.1.2), unlike B and C, the hotspots D to H do not change much when PCBM is added. Plus, their corresponding sizes are smaller than that of B and C in general. Based on these facts, it is likely that the hotspots D to I are in fact generated by the intramolecular structure, rather than the intermolecular structure as in the cases of B and C. It may be possible to identify what exact intramolecular structure each hotspot (D to H) corresponds to potentially, for example, by simulating diffraction signals using polymer models, although that is beyond the scope of this work and the subject of a separate study.

Another important point to note is the effect of the orientation of the ordered domains. While we detect the ordered domains from the dark-field images (e.g., Figure 3c), it is important to note that we are only detecting the domains that are oriented along the Bragg condition, and therefore,

https://doi.org/10.1021/acsami.4c11198
ACS Appl. Mater. Interfaces 2024, 16, 55852–55863

there are more ordered domains within our sample but they are not being captured in the images.[53] In addition, the speckle size in the diffraction pattern can broaden the size of the hotspots in the 2D histogram map. With a convergence angle of 2.5 mrad, the average size of speckles in the diffraction patterns at k = 2 nm^{-1} is around 0.2 nm^{-1} (as shown in the example map in Figure 2c). However, the relative change between P3HT and P3HT/PCBM is much greater than the magnitude of the broadening, which makes the comparison between the two maps (Figure 4c) still reliable.

3.1.2. Poly(3-hexylthiophene-2,5-diyl)/[6,6]-Phenyl C61 Butyric Acid Methyl Ester. Next, we examined the 2D histogram from the P3HT/PCBM blend (Figure 4b) and compared it to the case of P3HT-only that we showed in Figure 4a. While the hotspot positions in Figure 4a,b are generally similar (especially the ones that are at k > ∼2 nm^{-1}), they show a measurable degree of change, indicating that the nanoscale structure of the polymer blend changes when PCBM is incorporated. From Figure 4, the most changes are observed in A (nonexistent) → A′, B → B′ + A″, and C → C′, which highlight that the degree of both $\pi-\pi$ and alkyl ordering at the nanoscale in P3HT increases when PCBM is mixed in. First, for C → C′, the overall size of the $\pi-\pi$ hotspot did not change much, but the spot loses its "tail" (green oval) to the lower k in C′. The smaller range of k (due to the shortened tail) suggests that the degree of ordering of $\pi-\pi$ stacking in P3HT is enhanced (meaning the ordering is better defined in terms of their intermolecular spacing) when PCBM is mixed in. The $\pi-\pi$ distance is also slightly reduced in C′ (indicated by an increase in its k value, shown in Figure 4c), which indicates that the molecular ordering is more compact in C′. This change is described schematically in Figure 5. In the P3HT-only sample (Figure 5a), the ordered domains of $\pi-\pi$ stacking have a large variation of intermolecular spacing (indicated by the red arrow), which corresponds to the fact that the spot C in Figure 4a has a longer tail to the lower k. When PCBM incorporates (Figure 5b), the formation of PCBM domains (which will be explained below) may compress the P3HT domains to make them have shorter intermolecular spacing overall, which leads to a higher average k value and shorter tail to the low k in C′ as compared to C.

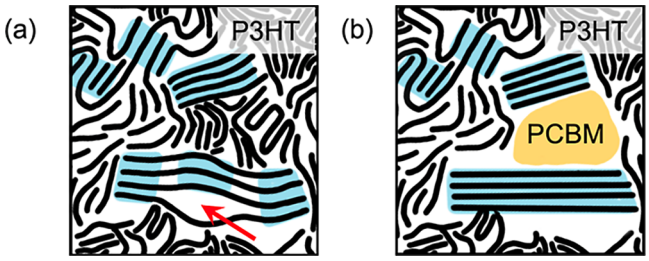

Figure 5. Schematic diagram showing (a) ordered domains in P3HT (highlighted in blue) and (b) how they become more closely packed and better ordered when PCBM is added. Additionally, the PCBM clusters can aid in the rearrangement of the P3HT chains, such as the region indicated by the red arrow in (a), which increases the overall size of the P3HT domains and decreases the stacking distance within the domain.

The addition of PCBM produces the most drastic changes in the 2D histograms in the low k regime (k < ∼2 nm^{-1}) due to the size of their clusters and internal ordering among PCBM molecules. We explain these changes by examining the center positions and the ranges of all hotspots from both P3HT (Figure 4a) and P3HT/PCBM (Figure 4b), which is shown in Figure 4c. The ranges of k and the size of the hotspots were determined by 2D Gaussian functions (both along the k and size dimension) that we fit to each of the hotspots.

First, the hotspots A′ (k = 1.19 nm^{-1}) and A″ (k = 2.23 nm^{-1}) can be identified as ordered PCBM nanoclusters since their peaks match the known peak positions of the PCBM crystal domains that produce peaks at ∼1.19 nm^{-1} and ∼2.29 nm^{-1}, according to GIWAXS data.[38,54,55] As shown in Figure 4c, these nanoclusters of PCBM have larger domain sizes (3.0 and 2.9 nm, respectively) as compared to hotspots C′−I′. This indicates that A (nonexistent) → A′ corresponds to a degree of donor−acceptor phase separation in our sample.[56,57] At the same time, hotspot B in Figure 4a experienced changes in its overall shape and location (B → B′ + A″). Since PCBM forms separated clusters, evidenced by the fact that A′ and A″ were created upon PCBM incorporation while P3HT domains remain in the 2D histogram, we can infer that B′ is P3HT while A″ corresponds to PCBM domains, even though there is no clear separation between B′ and A″.

As previously discussed, the degree of ordering of the polymer chains increases when the acceptor molecules are included in the thin film deposition solution. This means that, when B → B′, k slightly increases due to alkyl stacking distances getting more compact (intercalation or compression of side chains), but the overall size of the diffracting regions increases. This can be explained by the incorporation of neighboring ordered P3HT regions into a single one (increasing in size) aided by the addition of PCBM molecules, as shown in Figure 5 indicated by the red arrow.

For hotspots in the high k regime (k > ∼2 nm^{-1}), meaning hotspots D to I in Figure 4a, we observed that those hotspots are generally shifted to higher k when PCBM is incorporated (Figure 4c). While the ranges of the corresponding hotspots may overlap (e.g., between F and F′), the real-space distances corresponding to these hotspots are about 2−3 Å, which is smaller than typical chain stacking distances (either for $\pi-\pi$ or alkyl stacking), which indicates that these hotspots are rather corresponding to intramolecular information, such as the distance between side chains. In summary, the tendency for this system is that P3HT hotspots become smaller and have higher k (i.e., decreased intermolecular spacing that leads to increase in k) when PCBM is incorporated except at low k values. This indicates that the PCBM molecules appear to alter the less strict (larger spacing) ordering when mixed with P3HT as discussed for the C → C′ and B → B′ cases explained above, while making the P3HT domains with smaller spacing slightly smaller but also more compressed and ordered.

3.1.3. Symmetry and Degree of Ordering Analysis of P3HT and P3HT/PCBM Ordered Regions. Given the measurable changes shown in the 2D histogram upon the addition of PCBM molecules, angular correlation analysis was performed as discussed in Section 2.2.4 to gain symmetry information in addition to the stacking and real-space information obtained from the 2D histogram. Figure 6a,b shows the average angular correlations for both P3HT and P3HT/PCBM systems, respectively. Here, we can see that P3HT shows more well-defined 2-fold symmetry (hotspots located at φ = 180°), which represents the plane-like stacking of the molecules. In contrast, the P3HT/PCBM AC map shows a much weaker 2-fold signal. This is also apparent in Figure 6c, which shows the intensity profile across φ = 180° in

https://doi.org/10.1021/acsami.4c11198
ACS Appl. Mater. Interfaces 2024, 16, 55852−55863

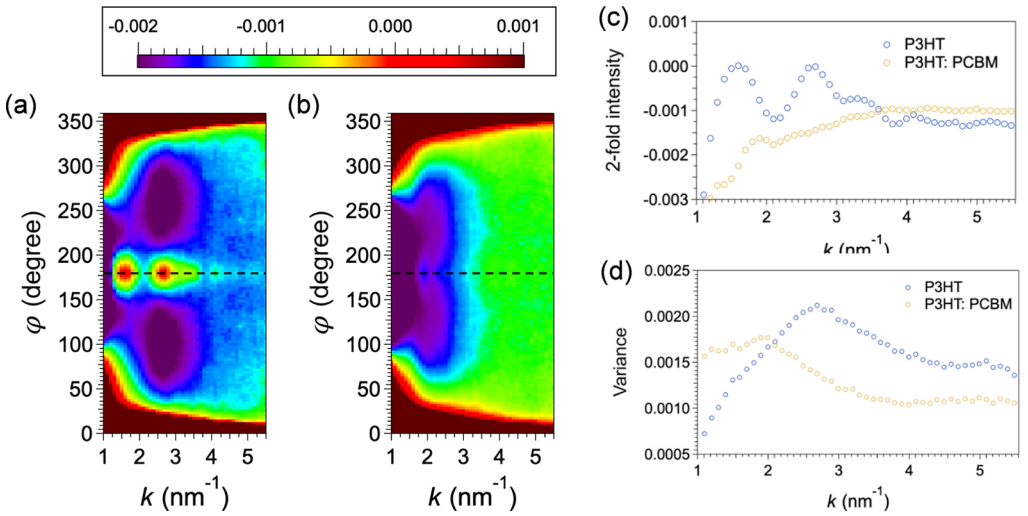

Figure 6. Angular correlation intensity indicated by the color bar for (a) P3HT and (b) P3HT/PCBM showing 2-fold symmetry. (c) 2-fold intensity profile at φ = 180° [dashed line in (a,b), respectively] and (d) variance of P3HT and P3HT/PCBM.

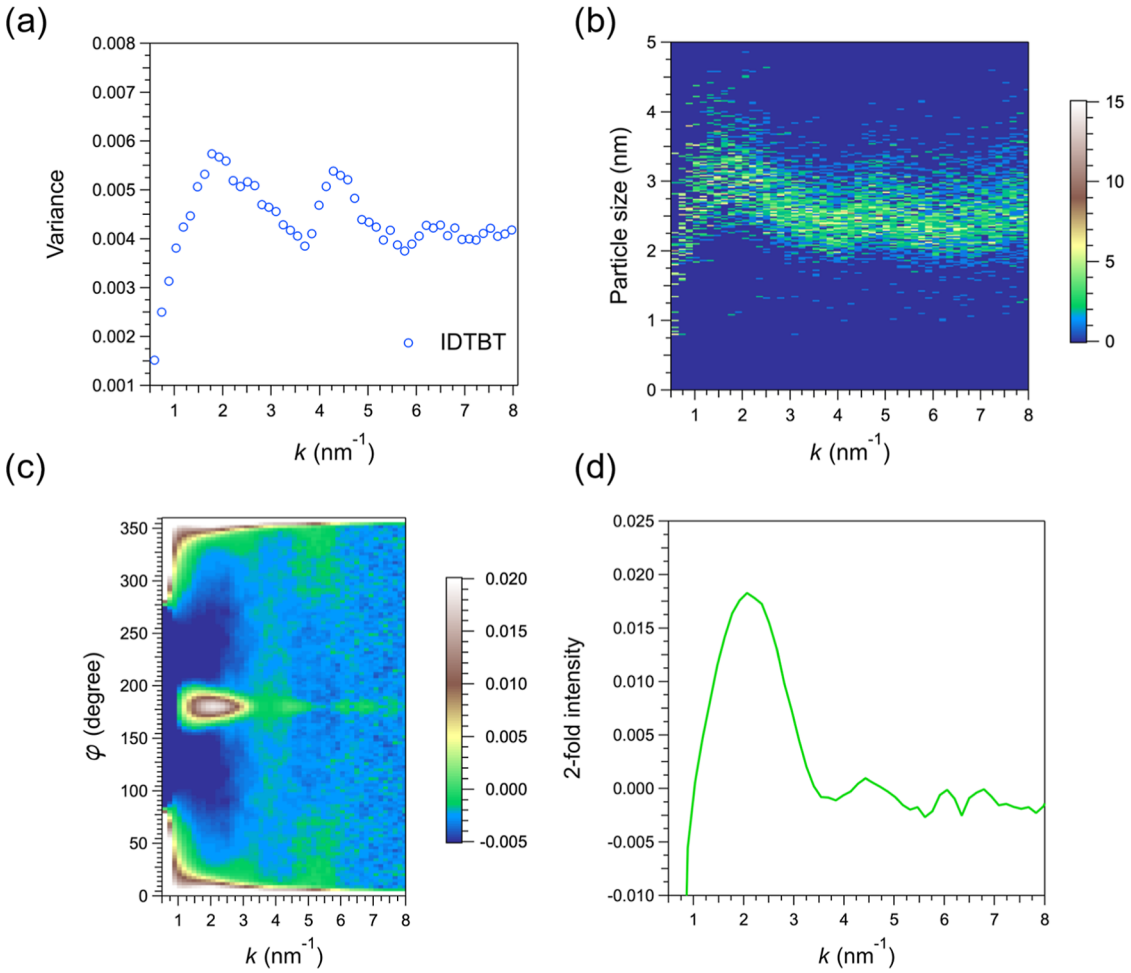

Figure 7. Analysis performed for IDTBT: (a) intensity variance, (b) 2D histogram, (c) angular correlation, and (d) profile at 180° of the angular correlation.

the angular correlation for both systems. The P3HT intensity profile at 180° shows clear peaks at 1.6 and 2.7 nm^{-1}, which correlates with hotspots B and C in the P3HT 2D histogram shown in Figure 4a. The presence of these peaks confirms that hotspots B and C correspond to alkyl and $\pi-\pi$ stacking, respectively, due to their k position and high degree of 2-fold symmetry. The 180° intensity profile corresponding to the P3HT/PCBM sample, the orange line shown in Figure 6c, shows that the 2-fold signal present in the P3HT is completely dampened by the addition of PCBM. Peaks at 1.6 and 2.7

https://doi.org/10.1021/acsami.4c11198
ACS Appl. Mater. Interfaces 2024, 16, 55852−55863

nm^{-1}, which corresponded to alkyl and $\pi-\pi$ stacking in P3HT as explained before, become significantly smaller in P3HT/PCBM. At the same time, a small peak at ~1.9 nm^{-1}, which correlates to A″ in Figure 4b, is shown in the profile. This suggests that PCBM nanoclusters only have a weak 2-fold symmetry. This can be explained by the fact that PCBM regions, although clustered, should not have high symmetry (e.g., such as 4- or 6-folds), as our in situ annealing temperature was 130 °C, which was lower than the reported crystallization temperature of 191 °C.[55] In addition, it should be noted that the $\pi-\pi$ peak in the P3HT profile is dampened in Figure 6c, even though the $\pi-\pi$ ordering is still present as indicated by the C′ spot in Figure 4b. This suggests that the spatial averaging process of the AC function loses the ability to differentiate the regions with P3HT versus PCBM, making the $\pi-\pi$ peak dampened by the PCBM regions.

Intensity variance in Figure 6d suggests that the signal from the P3HT ordered regions is affected by the addition of PCBM molecules. Both samples show the presence of broad peaks and similar intensity, although P3HT/PCBM has slightly lower intensity variance. The P3HT variance shows a broad peak at ~2.5 nm^{-1}, which corresponds to $\pi-\pi$ stacking (~2.6 nm^{-1}).[16] On the other hand, the data do not show any peaks for alkyl stacking, which we observed in the 2D histogram (Figure 4) at k ~ 1.2 nm^{-1} and 1.8 nm^{-1}. We believe this is mostly due to the fact that the variance is affected by multiple ordering domains (*i.e.*, hotspots in Figure 4a,b) that have the same k and bigger size, meaning that the structural information is compressed in one dimension in the variance data, essentially averaging over the size dimension of the 2D histogram. When the PCBM is added to the polymer blend, as shown in Figure 6d, the peaks present in the P3HT profile get significantly dampened, and a peak is formed at ~2 nm^{-1}, which is similar to the trend shown in the angular correlation results. While the variance shown here is relatively less informative compared to the angular correlation or the histogram map we presented earlier, the peaks in the variance data could be enhanced by using techniques such as cepstral analysis, which was demonstrated recently.[58]

Our conclusion for the P3HT and P3HT/PCBM taking into consideration results from the 2D histogram of domain size, angular correlation, and variance is that, when PCBM is mixed in, there is some degree of segregation between the donor (P3HT) and acceptor (PCBM) domains, and this segregation appears to make the P3HT ordering stricter and generate fullerene-rich domains that are bigger in size at low k values. Since the acquisition conditions were the same for both systems, this means that the amount of ordered P3HT regions was decreased upon the addition of PCBM. This is clearly indicated by the angular correlation measurement. Hence, the signal from the PCBM molecules dampens the signal from ordered regions, causing the disappearance of characteristic P3HT peaks in both angular correlation and variance. Similar behavior has been previously reported by X-ray diffraction characterization, in which alkyl and $\pi-\pi$ stacking peaks have disappeared from the spectrum.[55]

3.2. Indacenodithiophene-*co*-benzothiadiazole. The same analysis was also applied to IDTBT, and the results of intensity variance, 2D histogram, and angular correlation are shown in Figure 7, respectively. Variance (Figure 7a) shows distinct peaks at ~1.92 nm^{-1}, ~ 2.5 nm^{-1}, and ~4.28 nm^{-1}. While the first and second peak can be correlated to the alkyl stacking diffraction (1.9 nm^{-1}) and the $\pi-\pi$ stacking (2.45 nm^{-1}), the reported GIWAXS data does not extend to the higher k values collected in this data set.[15,32] Although the 2D histogram (Figure 7b) matches the overall trend of the variance, it does not show distinct hotspots, as P3HT showed in Figure 4a. This indicates that, unlike the case of P3HT, the structure of IDTBT at a ~2−3 nm length scale does not appear to separate into distinct ordering types, but instead, it shows a gradual and continuous molecular spacing variation throughout the scanned area. This continuous pattern in the 2D histogram is similar to what we observed in inorganic glasses and amorphous materials, where a similar constant change in medium range order distancing has been reported.[48,59] Angular correlation analysis (Figure 7c) shows strong intensity at k = 2 nm^{-1} with 2-fold symmetry (Figure 7d) that can be correlated to $\pi-\pi$ stacking.

The size of the ordered IDTBT domains, about 2−3 nm, is significantly smaller than what was observed in the recent phase-contrast HRTEM study of IDTBT by Cendra et al.[60] This raises an interesting point: not all ordered domains (represented by the phase-contrast fringes) observed in HRTEM images by Cendra et al. may diffract strongly enough to appear in our 4D-STEM dark-field images. In other words, it may be possible that the 4D-STEM dark-field images reported in our paper tend to capture regions with a higher degree of ordering than those observed by HRTEM. This conclusion aligns with the continuous change in molecular stacking distances that we measured in IDTBT. As the distances change, the effective domain size that we detect may become smaller (since one domain can be "disconnected" by the change in stacking distance), similar to the mechanism we illustrated in Figure 5.

To summarize, our study of IDTBT shows that this amorphous organic semiconductor has some ordering corresponding to in-plane diffraction along the backbone (k = 1.9 nm^{-1}) and $\pi-\pi$ stacking (k = 2.45 nm^{-1}). Nonetheless, it does not show distinct hotspots in the 2D histogram at the probed nanoscale level. The continuous intensity present in the 2D histogram regardless of the k value suggests a continuous change in molecular stacking distances.

4. CONCLUSIONS

We have demonstrated the application of 4D-STEM to quantitatively analyze nanoscale ordering in largely disordered organic semiconducting polymers. By utilizing a high dynamic range pixelated detector, we obtained statistically robust, high signal-to-noise ratio diffraction patterns from materials such as P3HT, P3HT/PCBM, and IDTBT. Our analysis techniques, including intensity variance, angular correlation, and 2D histogram analysis, allowed us to uncover detailed structural information about the molecular ordering within these polymers. We identified the characteristics of nanosized domains of alkyl and $\pi-\pi$ stacking in P3HT and measured the changes in molecular ordering when PCBM is incorporated, which leads to better-defined and more compact structures. For IDTBT, we observed a much lesser degree of ordering, indicating that this polymer does not exhibit distinct nanoscale domains such as in P3HT. The 4D-STEM analysis we report here represents a powerful tool for the detailed characterization of molecular ordering in organic semiconductors. This work not only enhances our understanding of these complex materials but also potentially paves the way for future innovations in organic electronics, contributing to the development of more efficient and reliable systems.

https://doi.org/10.1021/acsami.4c11198
ACS Appl. Mater. Interfaces 2024, 16, 55852−55863

AUTHOR INFORMATION

Corresponding Author

Jinwoo Hwang − *Department of Materials Science and Engineering, The Ohio State University, Columbus, Ohio 43212, United States;* orcid.org/0000-0002-5285-1128; Email: hwang.458@osu.edu

Authors

Gabriel A. Calderón Ortiz − *Department of Materials Science and Engineering, The Ohio State University, Columbus, Ohio 43212, United States*

Menglin Zhu − *Department of Materials Science and Engineering, The Ohio State University, Columbus, Ohio 43212, United States*

Andrew Wadsworth − *Department of Chemistry, Oxford University, Chemistry Research Laboratory, Oxford OX1 3TA, U.K.;* orcid.org/0000-0002-9050-0599

Letian Dou − *Davidson School of Chemical Engineering, Purdue University, West Lafayette, Indiana 47907, United States;* orcid.org/0000-0001-6411-8591

Iain McCulloch − *Department of Chemistry, Oxford University, Chemistry Research Laboratory, Oxford OX1 3TA, U.K.; Andlinger Center for Energy and the Environment and Department of Electrical and Computer Engineering, Princeton University, Princeton, New Jersey 08544, United States;* orcid.org/0000-0002-6340-7217

Complete contact information is available at: https://pubs.acs.org/10.1021/acsami.4c11198

Notes

The authors declare no competing financial interest.

ACKNOWLEDGMENTS

G.C.O and J.H. acknowledge partial support by the Center for Emergent Materials, the NSF-MRSEC under DMR-2011876. G.C.O and J.H. also would like to acknowledge the NanoSystems Laboratory at The Ohio State University for the spin-coating equipment that was utilized to make some of the P3HT samples used in this study. Electron microscopy was performed at the Center for Electron Microscopy and Analysis (CEMAS) at The Ohio State University.

REFERENCES

(1) Peng, Z.; Ye, L.; Ade, H. Understanding, Quantifying, and Controlling the Molecular Ordering of Semiconducting Polymers: From Novices to Experts and Amorphous to Perfect Crystals. *Mater. Horiz.* **2022**, *9*, 577−606.

(2) Noriega, R.; Rivnay, J.; Vandewal, K.; Koch, F. P. V.; Stingelin, N.; Smith, P.; Toney, M. F.; Salleo, A. A General Relationship between Disorder, Aggregation and Charge Transport in Conjugated Polymers. *Nat. Mater.* **2013**, *12*, 1038−1044.

(3) Olivier, Y.; Niedzialek, D.; Lemaur, V.; Pisula, W.; Mullen, K.; Koldemir, U.; Reynolds, J. R.; Lazzaroni, R.; Cornil, J.; Beljonne, D. 25th Anniversary Article: High-Mobility Hole and Electron Transport Conjugated Polymers: How Structure Defines Function. *Adv. Mater.* **2014**, *26* (14), 2119−2136.

(4) Sirringhaus, H.; Brown, P. J.; Friend, R. H.; Nielsen, M. M.; Bechgaard, K.; Langeveld-Voss, B. M. W.; Spiering, A. J. H.; Janssen, R. A. J.; Meijer, E. W.; Herwig, P.; de Leeuw, D. M. Two-Dimensional Charge Transport in Self-Organized, High-Mobility Conjugated Polymers. *Nature* **1999**, *401* (6754), 685−688.

(5) Wang, S.; Fabiano, S.; Himmelberger, S.; Puzinas, S.; Crispin, X.; Salleo, A.; Berggren, M. Experimental Evidence That Short-Range Intermolecular Aggregation Is Sufficient for Efficient Charge Transport in Conjugated Polymers. *Proc. Natl. Acad. Sci. U.S. Am.* **2015**, *112* (34), 10599−10604.

(6) Mollinger, S. A.; Krajina, B. A.; Noriega, R.; Salleo, A.; Spakowitz, A. J. Percolation Tie-Molecules, and the Microstructural Determinants of Charge Transport in Semicrystalline Conjugated Polymers. *ACS Macro Lett.* **2015**, *4* (7), 708−712.

(7) *Best Research-Cell Efficiency Chart*; Photovoltaic Research NREL. https://www.nrel.gov/pv/cell-efficiency.html (accessed Jul 5, 2024).

(8) Wang, L.; Guo, S.; Zhou, K.; Ma, W. Control of the Molecular Orientation in Small Molecule-Based Organic Photovoltaics. *Sustainable Energy Fuels* **2020**, *4* (10), 4934−4955.

(9) Na, J. Y.; Kang, B.; Park, Y. D. Influence of Molecular Weight on the Solidification of a Semiconducting Polymer during Time-Controlled Spin-Coating. *J. Phys. Chem. C* **2019**, *123* (28), 17102−17111.

(10) O'Hara, K.; Takacs, C. J.; Liu, S.; Cruciani, F.; Beaujuge, P.; Hawker, C. J.; Chabinyc, M. L. Effect of Alkyl Side Chains on Intercrystallite Ordering in Semiconducting Polymers. *Macromolecules* **2019**, *52* (7), 2853−2862.

(11) Untilova, V.; Biskup, T.; Biniek, L.; Vijayakumar, V.; Brinkmann, M. Control of Chain Alignment and Crystallization Helps Enhance Charge Conductivities and Thermoelectric Power Factors in Sequentially Doped P3HT:F4TCNQ Films. *Macromolecules* **2020**, *53* (7), 2441−2453.

(12) Memon, W. A.; Li, J.; Fang, Q.; Ren, Z.; Yan, S.; Sun, X. Synergistic Effect of Solvent and Epitaxy on the Formation of Anisotropic Structures of P3HT and P3HT/PCBM Films. *J. Phys. Chem. B* **2019**, *123* (33), 7233−7239.

(13) Lv, J.; Feng, Y.; Fu, J.; Gao, J.; Singh, R.; Kumar, M.; Kim, M.; Tang, H.; Lu, S.; Zhang, W.; McCulloch, I.; Li, J.; Kan, Z. Energetic Disorder and Activation Energy in Efficient Ternary Organic Solar Cells with Nonfullerene Acceptor Eh-IDTBR as the Third Component. *Sol. RRL* **2020**, *4* (3), 1900403.

(14) Yu, L.; Davidson, E.; Sharma, A.; Andersson, M. R.; Segalman, R.; Müller, C. Isothermal Crystallization Kinetics and Time−Temperature−Transformation of the Conjugated Polymer: Poly(3-(2′-Ethyl)Hexylthiophene). *Chem. Mater.* **2017**, *29* (13), 5654−5662.

(15) Zhang, X.; Bronstein, H.; Kronemeijer, A. J.; Smith, J.; Kim, Y.; Kline, R. J.; Richter, L. J.; Anthopoulos, T. D.; Sirringhaus, H.; Song, K.; Heeney, M.; Zhang, W.; McCulloch, I.; DeLongchamp, D. M. Molecular Origin of High Field-Effect Mobility in an Indacenodithiophene−Benzothiadiazole Copolymer. *Nat. Commun.* **2013**, *4*, 2238.

(16) Treat, N. D.; Shuttle, C. G.; Toney, M. F.; Hawker, C. J.; Chabinyc, M. L. In Situ Measurement of Power Conversion Efficiency and Molecular Ordering during Thermal Annealing in P3HT:PCBM Bulk Heterojunction Solar Cells. *J. Mater. Chem.* **2011**, *21* (39), 15224−15231.

(17) Gutt, C.; Grodd, L.; Mikayelyan, E.; Pietsch, U.; Kline, R. J.; Grigorian, S. Local Orientational Structure of a P3HT $\pi-\pi$ Conjugated Network Investigated by X-ray Nanodiffraction. *J. Phys. Chem. Lett.* **2014**, *5*, 2335−2339.

(18) Gilchrist, J. B.; Basey-Fisher, T. H.; Chang, S. C.; Scheltens, F.; McComb, D. W.; Heutz, S. Uncovering Buried Structure and Interfaces in Molecular Photovoltaics. *Adv. Funct. Mater.* **2014**, *24* (41), 6473−6483.

(19) Geiss, R. H. Electron Diffraction of Polymers. In *Encyclopedia of Polymer Science and Technology*; John Wiley & Sons, Ltd, 2014; pp 1−23..

(20) Takacs, C. J.; Treat, N. D.; Krämer, S.; Chen, Z.; Facchetti, A.; Chabinyc, M. L.; Heeger, A. J. Remarkable Order of a High-Performance Polymer. *Nano Lett.* **2013**, *13* (6), 2522−2527.

(21) Panova, O.; Chen, X. C.; Bustillo, K. C.; Ophus, C.; Bhatt, M. P.; Balsara, N.; Minor, A. M. Orientation Mapping of Semicrystalline Polymers Using Scanning Electron Nanobeam Diffraction. *Micron* **2016**, *88*, 30−36.

(22) Han, Y.; Nguyen, K.; Cao, M.; Cueva, P.; Xie, S.; Tate, M. W.; Purohit, P.; Gruner, S. M.; Park, J.; Muller, D. A. Strain Mapping of

Two-Dimensional Heterostructures with Subpicometer Precision. *Nano Lett.* **2018**, *18* (6), 3746−3751.
(23) Donohue, J.; Zeltmann, S. E.; Bustillo, K. C.; Savitzky, B.; Jones, M. A.; Meyers, G. F.; Ophus, C.; Minor, A. M. Cryogenic 4D-STEM Analysis of an Amorphous-Crystalline Polymer Blend: Combined Nanocrystalline and Amorphous Phase Mapping. *iScience* **2022**, *25* (3), 103882.
(24) Kuei, B.; Bator, C.; Gomez, E. D. Imaging 0.36 Nm Lattice Planes in Conjugated Polymers by Minimizing Beam Damage. *Macromolecules* **2020**, *53* (19), 8296−8302.
(25) Kuei, B.; Gomez, E. D. Pushing the Limits of High-Resolution Polymer Microscopy Using Antioxidants. *Nat. Commun.* **2021**, *12* (1), 153.
(26) Chen, M.; Bustillo, K. C.; Patel, V.; Savitzky, B. H.; Sternlicht, H.; Maslyn, J. A.; Loo, W. S.; Ciston, J.; Ophus, C.; Jiang, X.; Balsara, N. P.; Minor, A. M. Direct Imaging of the Crystalline Domains and Their Orientation in the PS-b-PEO Block Copolymer with 4D-STEM. *Macromolecules* **2024**, *57* (12), 5629−5638.
(27) Chatterjee, D.; Huang, S.; Gu, K.; Ju, J.; Yu, J.; Bock, H.; Yu, L.; Ediger, M. D.; Voyles, P. M. Using 4D STEM to Probe Mesoscale Order in Molecular Glass Films Prepared by Physical Vapor Deposition. *Nano Lett.* **2023**, *23* (5), 2009−2015.
(28) Tate, M. W.; Purohit, P.; Chamberlain, D.; Nguyen, K. X.; Hovden, R.; Chang, C. S.; Deb, P.; Turgut, E.; Heron, J. T.; Schlom, D. G.; Ralph, D. C.; Fuchs, G. D.; Shanks, K. S.; Philipp, H. T.; Muller, D. A.; Gruner, S. M. High Dynamic Range Pixel Array Detector for Scanning Transmission Electron Microscopy. *Microsc. Microanal.* **2016**, *22* (1), 237−249.
(29) Venkateshvaran, D.; Nikolka, M.; Sadhanala, A.; Lemaur, V.; Zelazny, M.; Kepa, M.; Hurhangee, M.; Kronemeijer, A. J.; Pecunia, V.; Nasrallah, I.; Romanov, I.; Broch, K.; McCulloch, I.; Emin, D.; Olivier, Y.; Cornil, J.; Beljonne, D.; Sirringhaus, H. Approaching Disorder-Free Transport in High-Mobility Conjugated Polymers. *Nature* **2014**, *515* (7527), 384−388.
(30) Nikolka, M.; Nasrallah, I.; Rose, B.; Ravva, M. K.; Broch, K.; Sadhanala, A.; Harkin, D.; Charmet, J.; Hurhangee, M.; Brown, A.; Illig, S.; Too, P.; Jongman, J.; McCulloch, I.; Bredas, J.-L.; Sirringhaus, H. High Operational and Environmental Stability of High-Mobility Conjugated Polymer Field-Effect Transistors through the Use of Molecular Additives. *Nat. Mater.* **2017**, *16* (3), 356−362.
(31) Li, G.; Shrotriya, V.; Huang, J.; Yao, Y.; Moriarty, T.; Emery, K.; Yang, Y. High-Efficiency Solution Processable Polymer Photovoltaic Cells by Self-Organization of Polymer Blends. *Nat. Mater.* **2005**, *4* (11), 864−868.
(32) Zhang, W.; Smith, J.; Watkins, S. E.; Gysel, R.; McGehee, M.; Salleo, A.; Kirkpatrick, J.; Ashraf, S.; Anthopoulos, T.; Heeney, M.; McCulloch, I. Indacenodithiophene Semiconducting Polymers for High-Performance, Air-Stable Transistors. *J. Am. Chem. Soc.* **2010**, *132* (33), 11437−11439.
(33) DeLongchamp, D. M.; Kline, R. J.; Herzing, A. Nanoscale Structure Measurements for Polymer-Fullerene Photovoltaics. *Energy Environ. Sci.* **2012**, *5* (3), 5980−5993.
(34) Karagiannidis, P. G.; Kassavetis, S.; Pitsalidis, C.; Logothetidis, S. Thermal Annealing Effect on the Nanomechanical Properties and Structure of P3HT:PCBM Thin Films. *Thin Solid Films* **2011**, *519* (12), 4105−4109.
(35) Egerton, R. F. Mechanisms of Radiation Damage in Beam-Sensitive Specimens, for TEM Accelerating Voltages between 10 and 300 KV. *Microsc. Res. Tech.* **2012**, *75*, 1550−1556.
(36) Savenije, T. J.; Kroeze, J. E.; Yang, X.; Loos, J. The Formation of Crystalline P3HT Fibrils upon Annealing of a PCBM:P3HT Bulk Heterojunction. *Thin Solid Films* **2006**, *511*−*512*, 2−6.
(37) Abdellah, A.; Virdi, K. S.; Meier, R.; Döblinger, M.; Müller-Buschbaum, P.; Scheu, C.; Lugli, P.; Scarpa, G. Successive Spray Deposition of P3HT/PCBM Organic Photoactive Layers: Material Composition and Device Characteristics. *Adv. Funct. Mater.* **2012**, *22* (19), 4078−4086.
(38) Drummy, L. F.; Davis, R. J.; Moore, D. L.; Durstock, M.; Vaia, R. A.; Hsu, J. W. P. Molecular-Scale and Nanoscale Morphology of P3HT:PCBM Bulk Heterojunctions: Energy-Filtered TEM and Low-Dose HREM. *Chem. Mater.* **2011**, *23* (3), 907−912.
(39) Yi, F.; Voyles, P. M. Effect of Sample Thickness, Energy Filtering, and Probe Coherence on Fluctuation Electron Microscopy Experiments. *Ultramicroscopy* **2011**, *111* (8), 1375−1380.
(40) Hwang, J.; Voyles, P. M. Variable Resolution Fluctuation Electron Microscopy on Cu-Zr Metallic Glass Using a Wide Range of Coherent STEM Probe Size. *Microsc. Microanal.* **2011**, *17* (1), 67−74.
(41) Hwang, J.; Melgarejo, Z. H.; Kalay, Y. E.; Kalay, I.; Kramer, M. J.; Stone, D. S.; Voyles, P. M. Nanoscale Structure and Structural Relaxation in Zr_{50} Cu_{45} A_5 Bulk Metallic Glass. *Phys. Rev. Lett.* **2012**, *108* (19), 195505.
(42) Im, S.; Chen, Z.; Johnson, J. M.; Zhao, P.; Yoo, G. H.; Park, E. S.; Wang, Y.; Muller, D. A.; Hwang, J. Direct Determination of Structural Heterogeneity in Metallic Glasses Using Four-Dimensional Scanning Transmission Electron Microscopy. *Ultramicroscopy* **2018**, *195*, 189−193.
(43) Gibson, J. M.; Treacy, M. M. J.; Sun, T.; Zaluzec, N. J. Substantial Crystalline Topology in Amorphous Silicon. *Phys. Rev. Lett.* **2010**, *105*, 125504.
(44) Treacy, M. M. J.; Gibson, J. M.; Fan, L.; Paterson, D. J.; McNulty, I. Fluctuation Microscopy: A Probe of Medium Range Order. *Rep. Prog. Phys.* **2005**, *68* (12), 2899−2944.
(45) Treacy, M. M. J.; Gibson, J. M. Variable Coherence Microscopy: A Rich Source of Structural Information from Disordered Materials. *Acta Crystallogr., Sect. A* **1996**, *52* (2), 212−220.
(46) Yavuz, I.; Zhang, L.; Briseno, A. L.; Houk, K. N. Simulations of Molecular Ordering and Charge-Transport of Oligo-Didodecylquaterthiophenes (DDQT). *J. Phys. Chem. C* **2015**, *119*, 158−165.
(47) Wochner, P.; Gutt, C.; Autenrieth, T.; Demmer, T.; Bugaev, V.; Ortiz, A. D.; Duri, A.; Zontone, F.; Grübel, G.; Dosch, H. X-Ray Cross Correlation Analysis Uncovers Hidden Local Symmetries in Disordered Matter. *Proc. Natl. Acad. Sci. U.S.A.* **2009**, *106* (28), 11511−11514.
(48) Im, S.; Wang, Y.; Zhao, P.; Yoo, G. H.; Chen, Z.; Calderon, G.; Abbasi Gharacheh, M.; Zhu, M.; Licata, O.; Mazumder, B.; Muller, D. A.; Park, E. S.; Wang, Y.; Hwang, J. Medium-Range Ordering, Structural Heterogeneity, and Their Influence on Properties of Zr-Cu-Co-Al Metallic Glasses. *Phys. Rev. Mater.* **2021**, *5* (11), 115604.
(49) Liu, Y. H.; Wang, D.; Nakajima, K.; Zhang, W.; Hirata, A.; Nishi, T.; Inoue, A.; Chen, M. W. Characterization of Nanoscale Mechanical Heterogeneity in a Metallic Glass by Dynamic Force Microscopy. *Phys. Rev. Lett.* **2011**, *106* (12), 125504.
(50) Liu, A. C. Y.; Bøjesen, E. D.; Tabor, R. F.; Mudie, S. T.; Zaccone, A.; Harrowell, P.; Petersen, T. C. Local Symmetry Predictors of Mechanical Stability in Glasses. *Sci. Adv.* **2022**, *8* (11), No. eabn0681.
(51) Bals, S.; Kabius, B.; Haider, M.; Radmilovic, V.; Kisielowski, C. Annular Dark Field Imaging in a TEM. *Solid State Commun.* **2004**, *130* (10), 675−680.
(52) Roels, J.; Vernaillen, F.; Kremer, A.; Gonçalves, A.; Aelterman, J.; Luong, H. Q.; Goossens, B.; Philips, W.; Lippens, S.; Saeys, Y. An Interactive ImageJ Plugin for Semi-Automated Image Denoising in Electron Microscopy. *Nat. Commun.* **2020**, *11* (1), 771.
(53) Stratton, W. G.; Voyles, P. M. A Phenomenological Model of Fluctuation Electron Microscopy for a Nanocrystal/Amorphous Composite. *Ultramicroscopy* **2008**, *108* (8), 727−736.
(54) Huq, A. F.; Ammar, A.; Al-Enizi, A. M.; Karim, A. In-Situ Orientation and Crystal Growth Kinetics of P3HT in Drop Cast P3HT:PCBM Films. *Polymer* **2017**, *113*, 200−213.
(55) Verploegen, E.; Mondal, R.; Bettinger, C. J.; Sok, S.; Toney, M. F.; Bao, Z. Effects of Thermal Annealing Upon the Morphology of Polymer−Fullerene Blends. *Adv. Funct. Mater.* **2010**, *20* (20), 3519−3529.
(56) Treat, N. D.; Brady, M. A.; Smith, G.; Toney, M. F.; Kramer, E. J.; Hawker, C. J.; Chabinyc, M. L. Interdiffusion of PCBM and P3HT Reveals Miscibility in a Photovoltaically Active Blend. *Adv. Energy Mater.* **2011**, *1* (1), 82−89.

(57) Parnell, A. J.; Cadby, A. J.; Mykhaylyk, O. O.; Dunbar, A. D. F.; Hopkinson, P. E.; Donald, A. M.; Jones, R. A. L. Nanoscale Phase Separation of P3HT PCBM Thick Films As Measured by Small-Angle X-Ray Scattering. *Macromolecules* **2011**, *44* (16), 6503−6508.
(58) Pidaparthy, S.; Ni, H.; Hou, H.; Abraham, D. P.; Zuo, J.-M. Fluctuation Cepstral Scanning Transmission Electron Microscopy of Mixed-Phase Amorphous Materials. *Ultramicroscopy* **2023**, *248*, 113718.
(59) Abbasi, M.; Dong, Y.; Meng, J.; Morgan, D.; Wang, X.; Hwang, J. In Situ Observation of Medium Range Ordering and Crystallization of Amorphous TiO2 Ultrathin Films Grown by Atomic Layer Deposition. *APL Mater.* **2023**, *11* (1), 11102.
(60) Cendra, C.; Balhorn, L.; Zhang, W.; O'Hara, K.; Bruening, K.; Tassone, C. J.; Steinrück, H. G.; Liang, M.; Toney, M. F.; McCulloch, I.; Chabinyc, M. L.; Salleo, A.; Takacs, C. J. Unraveling the Unconventional Order of a High-Mobility Indacenodithiophene−Benzothiadiazole Copolymer. *ACS Macro Lett.* **2021**, *10* (10), 1306−1314.

https://doi.org/10.1021/acsami.4c11198
ACS Appl. Mater. Interfaces 2024, 16, 55852−55863